Edelweiss Applied Science and Technology
ISSN: 2576-8484
Vol. 10, No. 4, 412-435
2026
Publisher: Learning Gate
DOI: 10.55214/2576-8484.v10i4.12674

Data-driven multi-objective optimization of explosively formed projectiles using central composite design

Vuong Mai Quoc[1], Dang Hoang Van[1], Quan Pham Hong[1*]
[1]Le Quy Don Technical University, 236 Hoang Quoc Viet, Ha Noi, Viet Nam; phquanstudying@lqdtu.edu.vn (Q.P.H.).

Abstract: The terminal ballistic performance of Explosively Formed Projectiles (EFP) is governed by highly non-linear interactions between liner geometry and explosive characteristics. To address this complexity, a rigorous multi-objective optimization framework is established by integrating the Box-Wilson Central Composite Design (CCD) with explicit dynamics simulations. The interactive effects of liner height (h/d), top thickness (δ_1/d), edge thickness (δ_2/d), and charge length (l/d) are systematically quantified. Numerical models, validated against static firing experiments, demonstrate high predictive reliability with relative errors consistently below 6%. Statistical analysis reveals that top thickness dictates kinematic performance, contributing over 98% to velocity variance, while an energy saturation plateau is identified at a charge length ratio of $l/d \approx 1.2$. Through constrained desirability optimization, an optimal configuration (h/d=0.221, δ_1/d=0.032, δ_2/d=0.012, l/d=1.215) is derived, achieving a terminal velocity of 2405 m/s, a penetration depth of 29.0 mm, and a hole diameter of 31.0 mm. Confirmatory simulations capture a significant dynamic necking effect at high velocities, effectively concentrating mass along the penetration axis and reducing target resistance. Consequently, the optimized projectile penetrates 24.4% deeper than statistical predictions and outperforms baseline designs by 34.9% in velocity, demonstrating the framework's efficacy for advanced warhead engineering.

Keywords: *Box-Wilson central composite design, Explosively formed projectile (EFP), Multi-objective optimization, Numerical simulation, Response surface methodology.*

1. Introduction

Explosively Formed Projectiles (EFP) constitute a critical class of directed-energy munitions, distinguished by their unique capability to defeat heavy armor and concrete fortifications from extended standoff distances through high-velocity kinetic energy transfer [1-3]. In contrast to shaped charge jets, which rely on high-velocity stretching mechanisms to achieve extreme penetration depths but are often susceptible to disruption by reactive armor systems [4, 5]. EFPs function by collapsing a shallow metallic liner into a compact, aerodynamically stable slug that retains high kinetic energy and structural integrity. The theoretical foundation for understanding these mechanics has been established through classical hydrodynamic models and further deepened by comprehensive studies on the physics of explosion and impact [1, 2, 5].

Historically, the optimization of EFP warheads involved extensive design trade-off analyses and relied heavily on semi-empirical guidelines [6, 7]. With the maturation of hydrocodes, numerical simulation has become the standard tool for investigating parametric sensitivities [8]. The fidelity of these simulations relies fundamentally on robust computational methods, such as Lagrangian and Eulerian schemes or Smoothed Particle Hydrodynamics (SPH) for complex fluid-structure interactions [9, 10]. Furthermore, precision in modeling requires rigorous mesh determination strategies [11], validation protocols to estimate modeling errors [12], and accurate material constitutive responses, specifically the Johnson-Cook model for metals and the JWL equation of state for high explosives [13, 14]. Currently, commercial solvers like ANSYS Autodyn are widely utilized for these nonlinear

History: Received: 20 January 2026; Revised: 25 March 2026; Accepted: 30 March 2026; Published: 13 April 2026
* Correspondence: phquanstudying@lqdtu.edu.vn

dynamic problems [15].

In recent years, the field has witnessed a paradigm shift from simple parametric sweeping to advanced computational optimization. Research has successfully optimized variable-thickness liners to enhance flight stability or utilized numerical design to reduce development costs [16, 17]. The application of statistical methods has also expanded significantly. For instance, orthogonal test methods have been applied to analyze the influence of multiple structural parameters on interior ballistics, demonstrating the efficiency of factorial designs [18]. Similarly, optimization algorithms have been utilized to enhance the ballistic impact resistance of multi-layered plates [19]. In the context of linear material processing, Response Surface Methodology (RSM) has been successfully deployed to optimize vacuum gradient heat treatment for copper alloys, achieving significant grain refinement and improved mechanical properties [20].

Despite these advances, a significant portion of EFP research still relies on "One-Factor-at-a-Time" approaches, which fail to capture synergistic interactions between design variables. To overcome this, Design of Experiments (DoE) methodologies are essential [21]. Statistical software tools have become instrumental in executing these rigorous analyses [22, 23]. While screening methods like the Taguchi design have been widely applied from injection molding to thermoelectric generation and incremental forming [24-26]. They are inherently limited to estimating linear effects. For precise optimization in a continuous and nonlinear design space, the Box-Wilson Central Composite Design (CCD) offers superior capability [27]. Unlike basic factorial designs, the Box-Wilson CCD incorporates axial points that allow for the estimation of quadratic curvature in the response surface, enabling the precise location of global optima. This approach has been validated in complex manufacturing simulations, such as projectile jacket optimization, and complements advanced structural methods like topology optimization for reactive materials [28, 29].

The theoretical framework for this Response Surface Methodology is comprehensively detailed in foundational statistical literature [30, 31]. The necessity of statistical rigor in such multivariate analyses to avoid overfitting is further emphasized in numerous studies [32-34]. Bridging the gap between theoretical hydrodynamics and advanced statistical optimization, this study proposes a rigorous framework integrating explicit dynamics simulations with the CCD. The research aims to systematically quantify the individual and interactive effects of four dimensionless parameters (h/d, δ_1/d, δ_2/d, l/d). The numerical model employed in this study is built upon and validated against recent experimental investigations, which successfully characterized the influence of liner top thickness, height, and curvature radii on the formation and penetration performance of EFP [35, 36].

2. Methodology

2.1. Projectile Geometry

To establish a rigorous design baseline, several geometric parameters of the warhead are held constant: the casing wall thicknesses are defined as t_1 = 4.4 mm and t_2 = 2.5 mm; the outer diameter of the casing is fixed at D = 54 mm; and the shared diameter for both the explosive and the liner base is set to d = 45.2 mm. Subject to these constraints, the optimization process focuses on a specific set of variable dimensions. These include the overall assembly length (L), the explosive charge length (l), and the structural characteristics of the liner: its thickness profile (δ_1, δ_2), inner and outer curvature radii (r_1, r_2), and liner height (h). As depicted in Figure , this entire configuration integrates a detonator, a C4 high-explosive charge, an OFHC copper liner, and a polyethylene casing.

Edelweiss Applied Science and Technology
ISSN: 2576-8484
Vol. 10, No. 4: 412-435, 2026
DOI: 10.55214/2576-8484.v10i4.12674

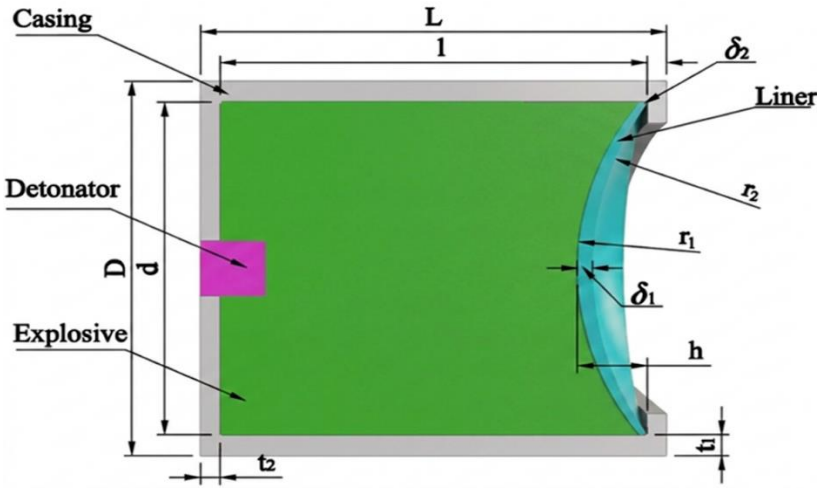

Figure 1.
EFP warhead model.

2.2. Material Constitutive Modeling and Numerical Framework

In this study, the complex thermo-mechanical behaviors of the warhead components under high-velocity shock loading were simulated using the high-fidelity explicit hydrocode ANSYS Autodyn-2D [15]. To ensure simulation fidelity, the constitutive models and Equation of State (EOS) were rigorously selected and calibrated based on specific thermodynamic characteristics. The isentropic expansion characteristics of the C4 high explosive detonation products were modeled using the Jones-Wilkins-Lee Equation of State (EOS). This standard formulation accurately predicts the detonation pressure based on relative volume and internal energy, ensuring precise energy coupling to the liner [8, 14, 15]:

$$P = A\left(1-\frac{\psi}{R_1V}\right)e^{-R_1V} + B\left(1-\frac{\psi}{R_2V}\right)e^{-R_2V} + \frac{\psi E}{V} \quad (1)$$

Where A, B, R_1, R_2, *and* ψ are empirically determined material constants, and E is the specific internal energy per unit volume [14, 15].

The polyethylene casing, subjected to large volumetric deformations under blast pressure, was modeled using a shock EOS [15, 37]. The linear relationship between shock velocity (U_s) and particle velocity (u_p) is defined as:

$$U_s = C_1 + S_1u_p \quad (2)$$

The pressure is subsequently calculated using the Mie-Grüneisen form, relating pressure to the internal energy E:

$$P = \frac{\rho_0 C_1^2 \mu\left[1+(1-\frac{\gamma_0}{2})\mu\right]}{\left[1-(S_1-1)\mu\right]^2} + \gamma_0 E \quad (3)$$

Where $\mu = \rho/\rho_0$ represents the compression ratio, C_1 is the Hugoniot slope coefficient [8, 15]. The 1006 steel target utilized the standard Johnson-Cook (JC) constitutive model coupled with a cumulative damage criterion to simulate the ductile perforation mechanism [13, 16].

For the OFHC copper liner, simulating severe plastic flow requires a constitutive law capable of addressing strain rates exceeding 10^4 s^{-1} alongside adiabatic thermal softening. Standard Johnson-Cook (JC) models often exhibit flow stress saturation at high strain rates, potentially leading to inaccuracies in predicting EFP tail formation [13]. Consequently, the Modified Johnson-Cook (MJC) model,

Edelweiss Applied Science and Technology
ISSN: 2576-8484
Vol. 10, No. 4: 412-435, 2026
DOI: 10.55214/2576-8484.v10i4.12674

proposed by Couque et al. [38] and validated for EFP simulations by Hussain et al. [39], was adopted. This model incorporates a viscous term to capture additional strain-rate hardening in the ultra-high strain rate regime [15, 38]:

$$\sigma_d = \left(A + B\varepsilon_p{}^n\right)\left(1 + C\ln\left(\frac{\varepsilon^*}{\varepsilon_\bullet^*}\right) + D\left(\frac{\varepsilon^*}{\varepsilon_l^*}\right)^k\right)\left[1 - T_c^m\right] \quad (4)$$

In which: σ_d – the dynamic yield stress; A, B, C, D n, m and k are the constants of the material determined experimentally; The term $D\left(\frac{\varepsilon^*}{\varepsilon_l^*}\right)^k$ represents the supplementary strengthening in the viscous regime, where is the reference transition strain rate (typically set at 10^3 s^{-1} for copper) [13, 15]; $T_c = \frac{T - T_{ref}}{T_{melt} - T_{ref}}$; T – the instantaneous temperature; T_{ref} – the initial temperature; T_{melt} – the melting temperature of the material.

The surrounding atmosphere is modeled as an ideal gas utilizing the Gamma-law Equation of State to capture shock wave transmission characteristics. The hydrostatic pressure P_a is defined as a function of the local density η and specific internal energy W [8, 15]:

$$P_a = \eta(\alpha - 1)\mathrm{W} \quad (5)$$

where the heat-capacity ratio is α = 1.4, under ambient conditions the density is η = 1.225 kg/m^3 and the specific internal energy is W =2.5 × 10^5 J/kg [8, 15].

The non-linear multi-physics dynamics were resolved using a coupled Euler-Lagrange strategy. The formation phase employed a multi-material Eulerian solver to mitigate mesh entanglement during the severe fluid-like inversion of the liner. Upon achieving a stable projectile geometry (at t= 0.75 ms), the state variables were remapped onto a Lagrangian grid to efficiently capture the history-dependent interactions during target penetration. The computational domain utilized flow-out boundary conditions to simulate an infinite medium, thereby eliminating spurious wave reflections that could corrupt the formation process. A critical critique in computational hydrodynamics is that finer mesh resolutions invariably yield superior accuracy. However, practical simulation requires establishing a solution independent of spatial discretization without incurring prohibitive computational costs. To address this, a rigorous mesh convergence study (grid independence test) was systematically executed on the critical explosive and liner domains, following established Verification and Validation (V&V) protocols [11, 40]. As illustrated in Fig. 2, three distinct mesh densities were evaluated: coarse (0.50 mm), medium (0.25 mm), and fine (0.125 mm). The analysis indicated that the coarse mesh (0.50 mm) was inadequate, exhibiting substantial numerical dissipation that resulted in an ill-defined projectile tail and an 8% deficit in predicted kinetic energy compared to the baseline. Conversely, while the fine mesh (0.125 mm) provided the highest geometric resolution, it imposed a severe penalty on computational efficiency. In explicit hydrocodes like Autodyn, the time step is strictly governed by the Courant-Friedrichs-Lewy (CFL) stability condition ($\Delta t \leq L_{min}/C$), implying that halving the element size necessitates halving the time step, which fundamentally leads to an exponential increase in total runtime [8, 15]. The results demonstrated that the medium mesh (0.25 mm) achieved an asymptotic convergence, yielding velocity and geometric predictions with discrepancies of less than 1.8% relative to the fine mesh, yet requiring only approximately 6.5% of the computational time. Consequently, a uniform element size of 0.25 mm x 0.25 mm was adopted as the optimal discretization standard, effectively balancing high-fidelity accuracy with the efficiency required for the subsequent multi-run optimization framework.

Edelweiss Applied Science and Technology
ISSN: 2576-8484
Vol. 10, No. 4: 412-435, 2026
DOI: 10.55214/2576-8484.v10i4.12674

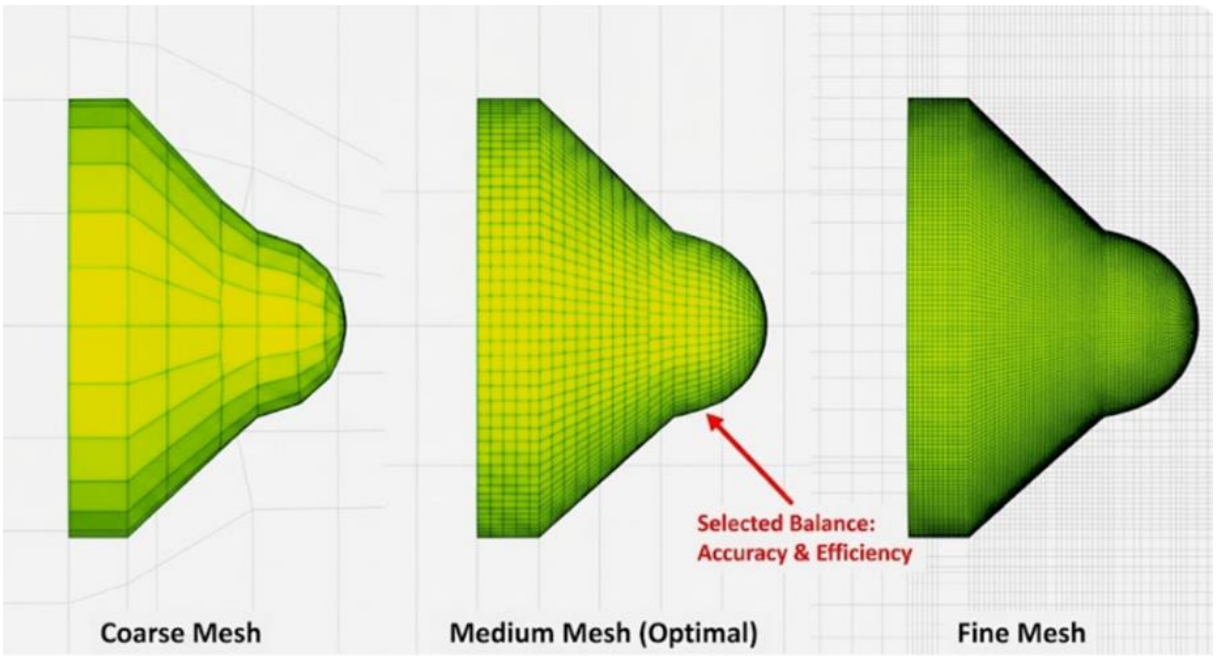

Figure 2.
Mesh convergence study and determination of optimal element size.

2.3. EFP Formation Dynamics and Numerical Simulation Principles

The formation of the EFP constitutes a complex thermo-mechanical phenomenon governed by the rapid interaction between high-pressure shock waves and the metallic liner, as shown in **Error! Reference source not found.**. Immediately upon initiation, the chemical potential energy of the explosive charge is converted into the kinetic energy of the detonation products, generating a shock front that propagates at high velocity and impacts the liner surface. Subjected to detonation pressures significantly exceeding the material's yield strength, the liner undergoes intense high-strain-rate plastic deformation, effectively transitioning from a solid state to a pseudo-fluid hydrodynamic behavior [1, 2].

The shaping mechanism is fundamentally driven by the inversion and convergence of the liner material towards the axis of symmetry. Due to the specific curvature of the liner, differential impulses are imparted to material elements at varying radial positions, establishing a non-uniform velocity field along the projectile axis. This axial velocity gradient acts as the critical determinant of formation quality: an optimally controlled gradient facilitates the stretching of the liner into a coherent, aerodynamically stable rod-like projectile. Conversely, if the velocity differential exceeds the material's dynamic ductility limits, critical instabilities such as necking and fragmentation will occur, severely compromising the terminal lethality [1, 6].

To rigorously model these non-linear physical phenomena, this study employs a multi-material Eulerian solver within a Finite Element framework. This computational approach robustly accommodates large mesh distortions and extensive material flow, thereby circumventing mesh entanglement issues inherent in traditional Lagrangian formulations [8, 9]. The simulation captures the transient evolution of the liner from its initial geometry to a stable aerodynamic equilibrium state, where the projectile attains its final morphology and velocity prior to target interaction. This stabilized configuration provides precise boundary conditions for subsequent penetration analysis, ensuring the continuity and fidelity of the integrated numerical model [3, 4].

Edelweiss Applied Science and Technology
ISSN: 2576-8484
Vol. 10, No. 4: 412-435, 2026
DOI: 10.55214/2576-8484.v10i4.12674

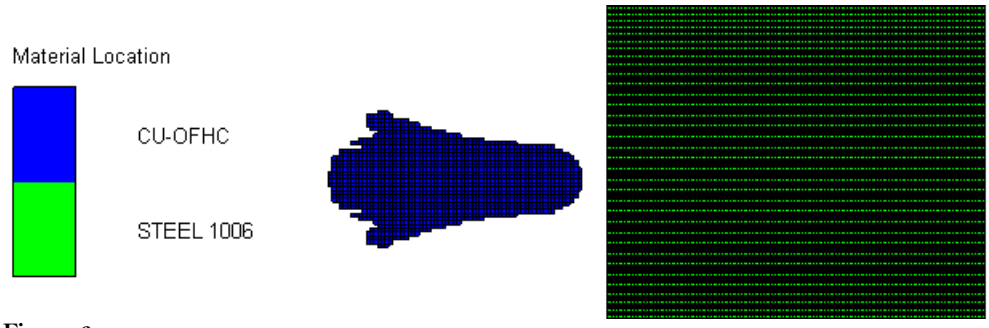

Figure 3.
The process of EFP formation.

2.4. EFP Impact Dynamics and Target Failure Mechanisms

To rigorously evaluate the terminal ballistic efficiency, the interaction between the stabilized EFP and the target plate is simulated using an Euler-to-Lagrange remapping technique, as shown in Fig. Upon achieving a coherent aerodynamic geometry, the projectile's state variables, comprising velocity vectors, stress tensors, and internal energy, are mapped onto a Lagrangian grid. This computational strategy leverages the Lagrangian solver's capability to accurately track material interfaces and history-dependent deformation, effectively mitigating the numerical diffusion artifacts often associated with Eulerian formulations at impact boundaries [8, 9].

Phenomenologically, the penetration process is governed by the projectile's high kinetic energy, which induces intense localized hydrodynamic pressures far exceeding the target material's yield strength. At the impact face, the target material flows radially outward under the penetrator's nose pressure, initiating a ductile hole growth mechanism. As the compressive shock front propagates through the target thickness and reflects off the rear free surface, it transforms into a tensile wave. This reflection induces a zone of high tensile stress at the distal face, potentially triggering spalling or scabbing failures due to the rapid elongation of the material [1, 2, 16].

To capture these complex thermo-mechanical behaviors, the target material is characterized using the Johnson-Cook constitutive and damage models. This formulation successfully captures strain-rate hardening and thermal softening effects within shear bands, accurately predicting the formation of a clean perforation channel consistent with experimental observations of through-hole formation [13, 16].

$$D_f = \sum \frac{\Delta\varepsilon}{\varepsilon^f} \tag{6}$$

$$\varepsilon^f = \left[D_1 + D_2 e^{D_3 \sigma^*} \right] \left[1 + D_4 \ln \dot{\varepsilon}_* \right] \left[1 + D_5 T_c \right] \tag{7}$$

Material failure in the steel plate is characterised by the Johnson–Cook damage model with constants D_1= 0.05, D_2= 4.22, D_3= -2.73, D_4= 0.0018, and D_5= 0.55 [35, 41, 42].

Edelweiss Applied Science and Technology
ISSN: 2576-8484
Vol. 10, No. 4: 412-435, 2026
DOI: 10.55214/2576-8484.v10i4.12674

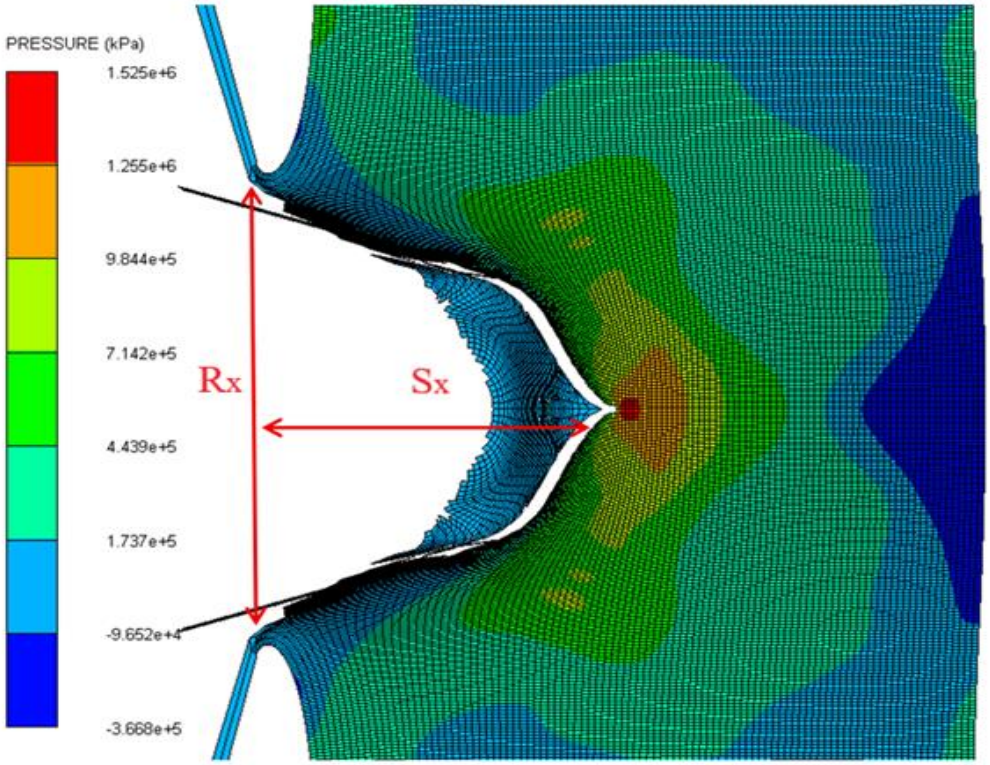

Figure 4.
Numerical simulation of terminal ballistics: Mesh deformation and pressure field during target perforation.

2.5. Validation of Numerical Model against Field Experiment

2.5.1. Experimental Setup and Test Configurations

To rigorously verify the fidelity of the numerical simulation framework (ANSYS Autodyn-2D) across different geometric regimes, a static firing test program was conducted using two distinct EFP warhead configurations, illustrated in

Fig. The first configuration (Case 1) corresponds to the center point of the design space, representing a variable-thickness liner ($\delta_1 > \delta_2$). The second configuration (Case 2) represents a uniform-thickness liner variant ($\delta_1 = \delta_2$) to assess the model's sensitivity to thickness gradients.
The specific geometric parameters for the test specimens are defined as follows:

- Case 1 (Variable Thickness): $h/d = 0.2$, $\delta_1/d = 0.044$, $\delta_2/d = 0.022$, and $l/d = 1.2$.
- Case 2 (Uniform Thickness): $h/d = 0.2$, $\delta_1/d = 0.044$, $\delta_2/d = 0.044$, and $l/d = 1.2$.

Edelweiss Applied Science and Technology
ISSN: 2576-8484
Vol. 10, No. 4: 412-435, 2026
DOI: 10.55214/2576-8484.v10i4.12674

Figure 5.
EFP warhead and steel target.

The liners were CNC-machined from OFHC copper, and the warheads utilized C4 plastic explosive initiated by a No. 8 electric detonator. The experimental setup, shown in Figure , positioned the warhead at a stand-off distance of 3.0 m from a 20 mm thick steel target. Projectile velocity was captured using a high-precision UTC-8 electronic timer with break-screens located at 2.0 m and 3.0 m from the charge face.

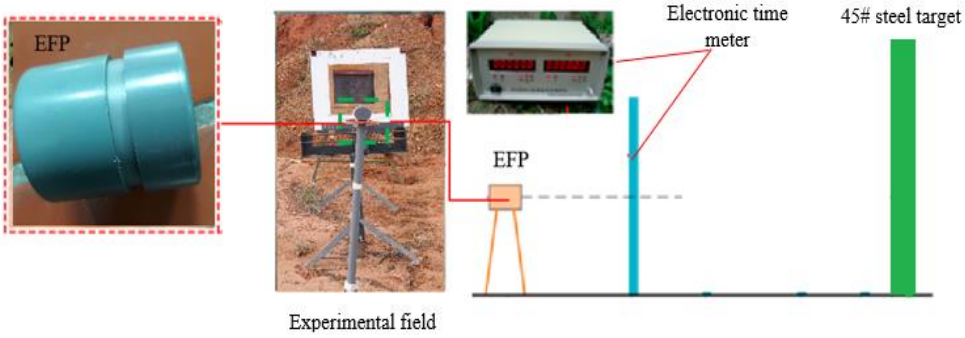

Figure 6.
Experimental measurement of EFP velocity and hole diameter.

2.5.2. Experimental Results

To rigorously evaluate the predictive fidelity of the numerical simulation framework, the results obtained from static firing tests were systematically compared against Autodyn-2D predictions. The evaluation process follows a logical progression from morphological inspection to quantitative data analysis and trend validation.

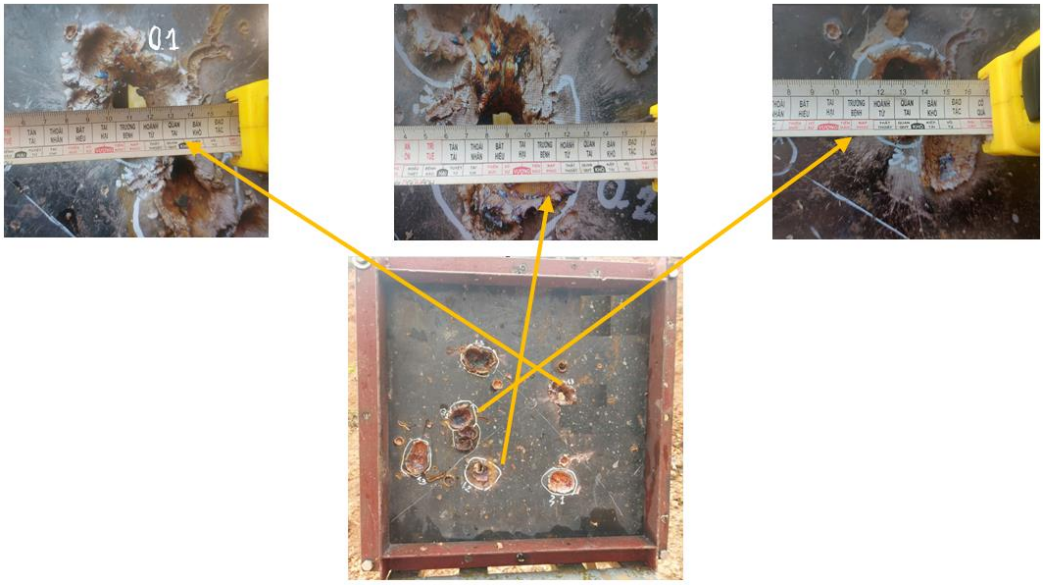

Figure 7.
Experimental validation of the simulation model.

First, the physical damage morphologies on the steel targets are visualized in Fig. The recovered specimens confirm that both warhead configurations successfully achieved complete perforation of the

Edelweiss Applied Science and Technology
ISSN: 2576-8484
Vol. 10, No. 4: 412-435, 2026
DOI: 10.55214/2576-8484.v10i4.12674

20 mm steel plates. The visual evidence clearly distinguishes between the impact characteristics of the two designs: the variable-thickness liner (Case 1) produced a clean, consistent perforation channel typical of a stable slug, whereas the uniform-thickness liner (Case 2) resulted in a different penetration footprint, verifying the influence of liner geometry on terminal ballistics.

Quantitatively, the specific kinematic and damage metrics are summarized in Table 1. For the baseline variable-thickness design (Case 1), the experiments yielded an average muzzle velocity (V) of 2096 m/s and a hole diameter (Rx) of 37.7 mm. Correspondingly, the numerical simulation predicted a velocity of 1981 m/s and a hole diameter of 36.0 mm. For the uniform-thickness variant (Case 2), the experimental measurements recorded a velocity of 1783 m/s and a hole diameter of 26.3 mm, while the simulation output was 1872 m/s and 29.0 mm, respectively.

Table 1.
Comparison between Field Experiment and Simulation (Baseline Case).

Configuration	Parameter	Experiment (Avg.)	FEM Simulation	Error (Exp vs FEM)
Case 1	V (m/s)	2096	1981	5.8%
	R_x (mm)	37.7	36	4.72%
Case 2	V (m/s)	1783	1872	4.75%
	R_x (mm)	26.3	29	9.31%

Finally, the correlation between the experimental measurements and numerical predictions is graphically presented in Fig. The comparative plots demonstrate that the numerical solver accurately captures the performance shifts induced by geometric variations. As indicated by the data in Table 1, the relative error for velocity in Case 1 is approximately 5.8%, and the hole diameter deviation is 4.72%. This close convergence validates that the established computational model is sufficiently robust and reliable to serve as the foundation for subsequent optimization studies.

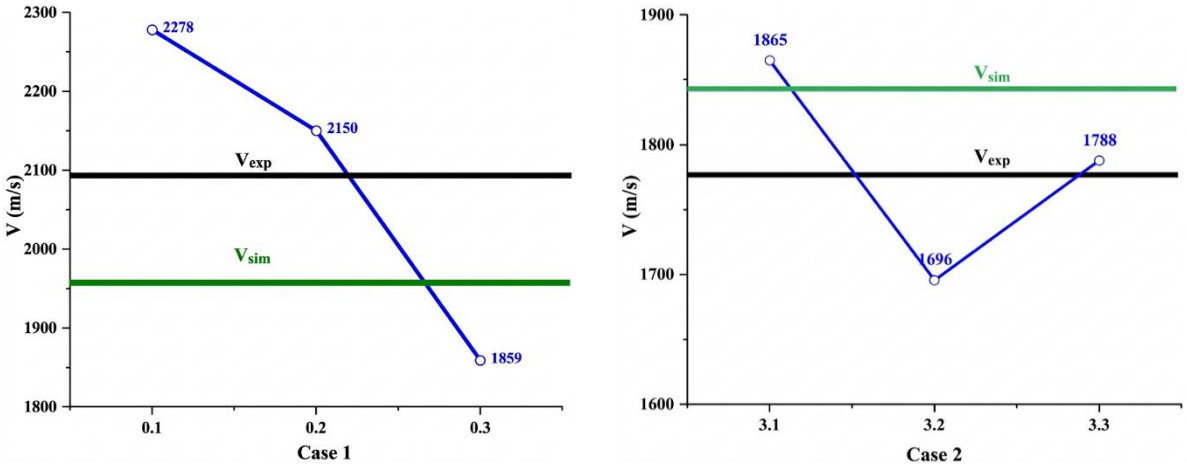

Edelweiss Applied Science and Technology
ISSN: 2576-8484
Vol. 10, No. 4: 412-435, 2026
DOI: 10.55214/2576-8484.v10i4.12674

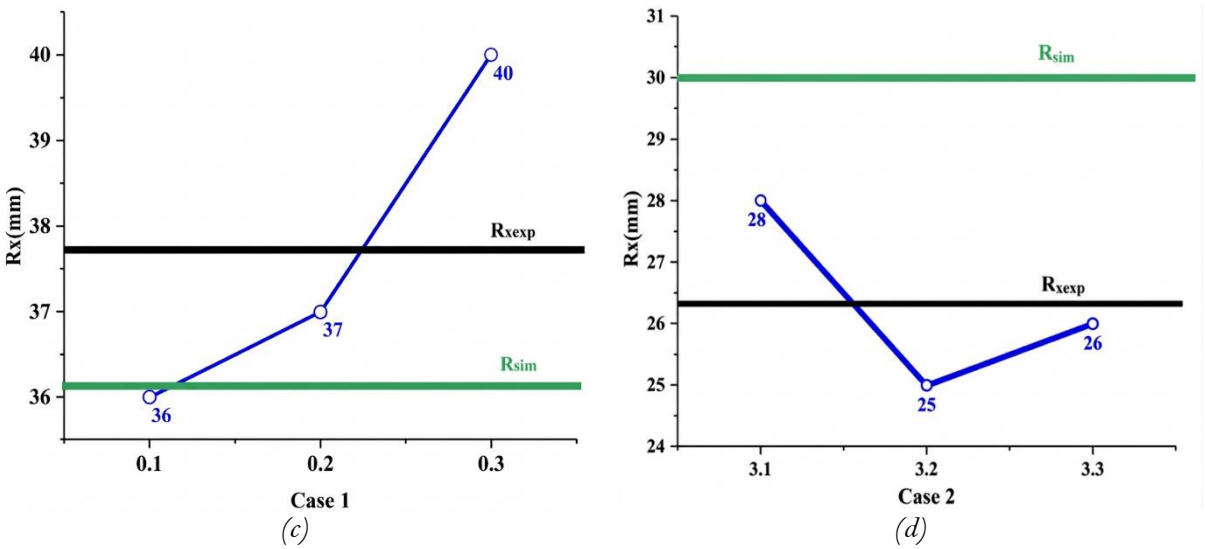

Figure 8.
Comparison of Experimental and Numerical results for Projectile Velocity and Hole Diameter

2.6. Experimental Design and Hybrid Optimization Strategy

2.6.1. Scientific Rationale for the Center Point Selection

The selection of the center point for the Box-Wilson design, defined as vector $C_0 = [h/d = 0.2, \delta_1/d = 0.044, \delta_2/d = 0.022, l/d = 1.2]$, is predicated on a convergence of fundamental hydrodynamic theories and validated parametric boundaries established in recent literature.

Regarding the liner geometry, the dimensionless height (h/d) serves as the critical bifurcation parameter between jetting and slug formation. While classical theories delineate the broad transition zones based on cone angle and height, recent numerical investigations have specifically refined the optimal window for EFP applications to the range of $0.2 \leq h/d \leq 0.3$ [1, 2, 36]. Within this domain, a baseline value of 0.2 was selected to prioritize a compact warhead configuration while ensuring sufficient standoff capability without inducing necking instabilities associated with excessive elongation [36].

Simultaneously, the mass distribution profile governs the kinetic energy transfer and structural survivability of the projectile. Analytical models for linear acceleration and recent sensitivity analyses have empirically narrowed the feasible top thickness (δ_1/d) to a range of 0.03-0.05 [2, 35]. Consequently, a value of 0.044 was identified as the equilibrium point that maximizes axial velocity while providing adequate inertial confinement to prevent shock-induced fragmentation [35]. Furthermore, to facilitate aerodynamic stability, a variable thickness strategy is essential. Adhering to recommendations on tapering thickness distributions ($\delta_1/d > \delta_2/d$), the edge thickness was set to 0.022, establishing a 2:1 ratio to induce a controlled velocity differential along the liner meridian, thereby promoting the formation of a streamlined, rod-like penetrator rather than a dispersed slug [16, 35].

Finally, the explosive charge dimension is constrained by the thermodynamic limits of energy coupling. Hydrodynamic studies indicate that the kinetic energy gain exhibits a saturation plateau when the charge length-to-diameter ratio (l/d) exceeds the range of 1.1 to 1.4 [40]. Extending the charge beyond this limit yields diminishing returns in velocity while introducing parasitic weight. Therefore, a value of 1.2 was conservatively chosen as the center point, positioned at the onset of this saturation zone to ensure maximal detonation impulse efficiency [40]. By integrating these physical constraints, the selected C_0 provides a scientifically robust baseline for subsequent response surface optimization.

Edelweiss Applied Science and Technology
ISSN: 2576-8484
Vol. 10, No. 4: 412-435, 2026
DOI: 10.55214/2576-8484.v10i4.12674

2.6.2. Box-Wilson Central Composite Design (CCD)

To rigorously quantify the non-linear interactions and quadratic curvature inherent in the EFP formation process, the Box-Wilson Central Composite Design (CCD) was employed [27, 30]. This second-order design offers a distinct advantage over first-order screening methods, such as the standard Taguchi L_{16}, by enabling precise mapping of the response surface topology and the identification of interior stationary points for global optimization [21].

As illustrated in Fig. 9, the CCD geometry is constructed from three distinct types of experimental points. The design is anchored by the factorial points (2^k), depicted as black circles at the vertices of the hypercube; these points are essential for estimating the linear main effects and two-way interactions within the coded levels (± 1). To resolve the response surface curvature and calculate the pure quadratic coefficients (β_{ii}), the matrix is augmented with axial points (or 'star' points, shown as red triangles), positioned along the coordinate axes at a specific distance α from the center. Additionally, replicate center points (blue squares) are located at the origin to estimate the pure experimental error and assess the goodness-of-fit (adequacy) of the second-order model [30].

This CCD configuration is rotatable, ensuring the prediction variance depends solely on the distance from the design center, independent of direction. This isotropic prediction precision is illustrated by the circumscribed sphere (green dashed lines) in Fig. 9. For a four-factor experiment (k=4), the rotatability condition is satisfied by setting the axial distance $\alpha = (2^k)^{1/4} = 2$. Consequently, the complete experimental matrix aggregates to $N = 2^k + 2k + n_c = 16 + 8 + 3 = 27$ independent simulation runs. This structure provides a statistically efficient framework for deriving the second-order polynomial regression equations with uniform precision throughout the spherical design space [27, 30].

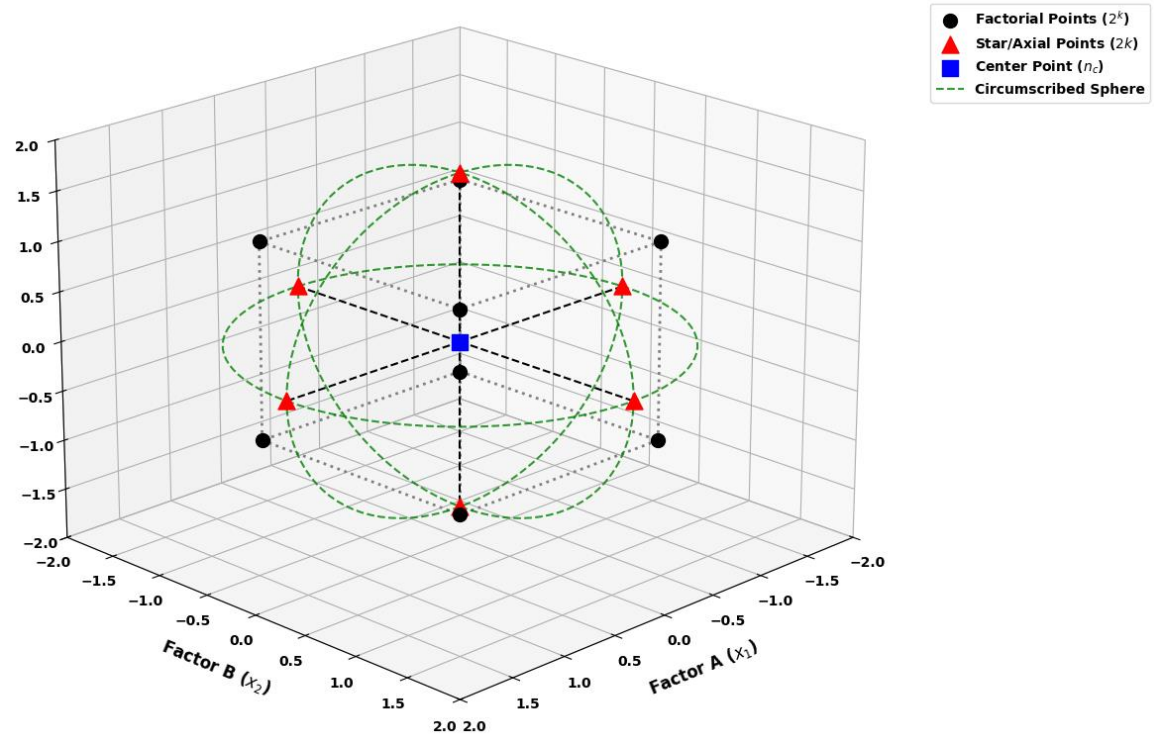

Figure 9.
Schematic representation of the Box-Wilson Central Composite Design.

Edelweiss Applied Science and Technology
ISSN: 2576-8484
Vol. 10, No. 4: 412-435, 2026
DOI: 10.55214/2576-8484.v10i4.12674

3. Results and Discussion

3.1. Design of Experiment Results and Morphological Analysis

The complete experimental design matrix, executed according to the Box-Wilson CCD framework, comprises 27 independent simulation runs. The specific geometric configurations for each run, defined by their physical dimensions (h/d, δ_1/d, δ_2/d, l/d), along with the recorded numerical responses for Muzzle Velocity (V), Hole Diameter (R_x), and Penetration Depth (S_x), are detailed in Table 2.

Table 2.
Box-Wilson Central Composite Design Matrix and Simulation Results.

No.	Type	h/d	δ_1/d	δ_2/d	l/d	V (m/s)	R_x (mm)	S_x (mm)
1	Factorial	0.18	0.033	0.017	1.15	2327	38	17
2	Factorial	0.22	0.033	0.017	1.15	2285	35	23
3	Factorial	0.18	0.055	0.017	1.15	1765	40	15
4	Factorial	0.22	0.055	0.017	1.15	1693	40	18
5	Factorial	0.18	0.033	0.027	1.15	2281	38	15
6	Factorial	0.22	0.033	0.027	1.15	2246	30	22
7	Factorial	0.18	0.055	0.027	1.15	1711	42	11
8	Factorial	0.22	0.055	0.027	1.15	1665	42	16
9	Factorial	0.18	0.033	0.017	1.25	2359	38	18
10	Factorial	0.22	0.033	0.017	1.25	2353	38	23
11	Factorial	0.18	0.055	0.017	1.25	1799	41	14
12	Factorial	0.22	0.055	0.017	1.25	1735	40	19
13	Factorial	0.18	0.033	0.027	1.25	2303	40	15
14	Factorial	0.22	0.033	0.027	1.25	2288	32	22
15	Factorial	0.18	0.055	0.027	1.25	1747	42	11
16	Factorial	0.22	0.055	0.027	1.25	1699	41	17
17	Center	0.20	0.044	0.022	1.20	1982	38	21
18	Center	0.20	0.044	0.022	1.20	1982	38	21
19	Center	0.20	0.044	0.022	1.20	1982	38	21
20	Axial	0.16	0.044	0.022	1.20	2011	40	12
21	Axial	0.24	0.044	0.022	1.20	1931	36	25
22	Axial	0.20	0.022	0.022	1.20	2787	34	16
23	Axial	0.20	0.066	0.022	1.20	1537	40	15
24	Axial	0.20	0.044	0.012	1.20	1982	40	22
25	Axial	0.20	0.044	0.032	1.20	1929	40	16
26	Axial	0.20	0.044	0.022	1.10	1931	40	17
27	Axial	0.20	0.044	0.022	1.30	2009	40	19

The data reveals a substantial spread in performance metrics across the design space, confirming that the selected parameter ranges effectively capture the critical transition zones of EFP formation. Muzzle velocity (V) exhibits the widest variation, ranging from a minimum of 1537 m/s (Run 23) to a high-velocity peak of 2787 m/s (Run 22). This extreme contrast highlights the dominant influence of the liner top thickness (δ_1/d); Run 22, with the thickness δ_1/d = 0.022, achieved maximum acceleration due to reduced inertial mass, whereas Run 23, with the thickness δ_1/d = 0.066, suffered from significant velocity retardation.

Penetration depth (S_x) also shows significant sensitivity, varying between 11 mm and 25 mm. Notably, the deepest penetration (25 mm) was observed in Run 21, which corresponds to the highest liner height (h/d = 0.24). This suggests that while velocity is crucial, the available penetrator mass and length, governed by the initial liner height, are equally vital for hydrodynamic penetration into steel targets. The hole diameter (R_x) remained relatively stable, fluctuating between 30 mm and 42 mm, indicating that radial expansion is less sensitive to geometric perturbations than axial elongation.

The replicate Center Points (Runs 17, 18, and 19) demonstrated perfect consistency (V=1982 m/s, S_x=21 mm), validating the numerical stability of the Autodyn solver. Meanwhile, the Axial Points

Edelweiss Applied Science and Technology
ISSN: 2576-8484
Vol. 10, No. 4: 412-435, 2026
DOI: 10.55214/2576-8484.v10i4.12674

successfully mapped the quadratic curvature of the response surface, revealing the nonlinear tradeoffs that simple linear screening would miss. For instance, increasing the charge length from l/d=1.1 (Run 26) to l/d=1.3 (Run 27) yielded a diminishing return in velocity (1931 m/s to 2009 m/s), hinting at the energy saturation plateau predicted by hydrodynamic theory. These morphological transitions and parametric sensitivities provide a robust dataset for subsequent regression modeling.

3.2. Statistical Model Validation and Refinement

The experimental data derived from the Box-Wilson Central Composite Design was analyzed to quantify the influence of liner height (h/d), top thickness (δ_1/d), edge thickness (δ_2/d), and charge length (l/d) on three key performance metrics: muzzle velocity (V), hole diameter (R_x), and penetration depth (S_x). To ensure model parsimony and predictive robustness, a backward elimination procedure was employed with a significance threshold of $\alpha = 0.1$. Statistically insignificant terms were iteratively removed to improve the goodness-of-fit over the initial full models.

Table 3 summarizes the statistical metrics and significant coefficients for the reduced models. The velocity model (V) demonstrates exceptional precision with an adjusted determination coefficient (R^2_adj) of 99.72% and a minimal standard error (S=15.46). The penetration depth model (S_x) also shows high reliability (R^2_adj of 88.27%), identifying significant nonlinear quadratic effects. The hole diameter model (R_x), while inherently more stochastic due to complex target interaction mechanisms, achieves a satisfactory R^2_adj of 76.00% by retaining critical two-way interaction terms.

Based on these validated statistics, the explicit second-order regression equations (in uncoded units) were established as follows:

Muzzle Velocity Model (V):

$$V = 3407 + 633\left(\frac{h}{d}\right) - 52589\left(\frac{\delta_1}{d}\right) - 4983\left(\frac{\delta_2}{d}\right) + 388.3\left(\frac{l}{d}\right) + 376017\left(\frac{\delta_1}{d}\right)^2 - 37500\left(\frac{h}{d}\cdot\frac{\delta_1}{d}\right) \quad ((8)$$

Hole Diameter Model (R_x):

$$R_x = 66.0 - 94\left(\frac{h}{d}\right) - 1148\left(\frac{\delta_1}{d}\right) + 850\left(\frac{\delta_2}{d}\right) + 4830\left(\frac{h}{d}\cdot\frac{\delta_1}{d}\right) - 8125\left(\frac{h}{d}\cdot\frac{\delta_2}{d}\right) + 17045\left(\frac{\delta_1}{d}\cdot\frac{\delta_2}{d}\right) \quad ((9)$$

Penetration Depth Model (S_x):

$$S_x = -618 + 896\left(\frac{h}{d}\right) + 955\left(\frac{\delta_1}{d}\right) + 850\left(\frac{\delta_2}{d}\right) + 845\left(\frac{l}{d}\right) - 1875\left(\frac{h}{d}\right)^2 - 12397\left(\frac{\delta_1}{d}\right)^2 - 25000\left(\frac{\delta_2}{d}\right)^2 - 350\left(\frac{l}{d}\right)^2 \quad ((10)$$

Edelweiss Applied Science and Technology
ISSN: 2576-8484
Vol. 10, No. 4: 412-435, 2026
DOI: 10.55214/2576-8484.v10i4.12674

Table 3.
Summary of ANOVA results and regression coefficients for the optimized EFP models.

Factors & Statistics	Velocity (V)	Hole Diameter (Rx)	Penetration Depth (Sx)
Model Adequacy			
Adjusted (R^2)	99.72%	76.00%	88.27%
Standard Error (S)	15.46	1.45	1.30
Coded Coefficients (β)			
Constant (β_0)	1974.35	38.61	21.25
h/d	-20.33 ***	-1.21 **	+2.92 ***
δ_1/d	-297.00 ***	+2.13 ***	-1.50 ***
δ_2/d	-24.92 ***	-0.13 ns	-1.25 ***
l/d	+19.42 ***	-	+0.25 ns
Quadratic Terms			
$(h/d)^2$	-	-	-0.75 *
$(\delta_1/d)^2$	+45.50 ***	-	-1.50 ***
$(\delta_2/d)^2$	-	-	-0.63 *
$(l/d)^2$	-	-	-0.88 **
Interaction Terms			
h/d x δ_1/d	-8.25 *	+1.06 **	-
h/d x δ_2/d	-	-0.81 *	-
δ_1/d x δ_2/d	-	+0.94 *	-

Note: The regression coefficients are derived based on coded factor levels ranging from -2 to +2. Statistical significance is denoted by asterisks, where triple asterisks (***) indicate a highly significant effect ($P < 0.001$), double asterisks (**) represent a significant effect ($P < 0.01$), and a single asterisk (*) indicates statistical significance at the $P < 0.05$ level. Terms marked as 'ns' are statistically insignificant ($P > 0.1$) but are retained to preserve the hierarchical integrity of the second-order model.

3.3. Parametric Influence and Design Trade-Offs

3.3.1. Effect of Liner Height

Liner height presents a classic design conflict between speed and lethality. Increasing *h/d* introduces a drag penalty on velocity (β = -20.33) due to added mass. Conversely, it is the strongest positive driver for penetration depth (β = +2.92), confirming that a taller liner provides the necessary material volume to form a high-aspect-ratio rod capable of deep target perforation. Therefore, the optimal *h/d* must be selected to balance momentum retention (mass) against initial velocity.

3.3.2. Effect of Liner Top Thickness

The analysis identifies the liner top thickness as the governing factor for EFP kinematics. For velocity (V), δ_1/d exerts an overwhelming negative influence (β= -297.00), where thinning the liner apex significantly boosts acceleration. However, a crucial trade-off is observed: while decreasing δ_1/d maximizes velocity, it simultaneously reduces the hole diameter (R_x, β= +2.13) and penetration depth (S_x, β= -1.50). This implies that an excessively thin liner top produces a fast but potentially smaller and less effective penetrator. The quadratic nature of its effect on velocity ($P < 0.001$) further suggests performance gains accelerate as the thickness approaches the lower structural limit.

3.3.3. Effect of Edge Thickness

Unlike the other parameters, the edge thickness (δ^2/d) does not exhibit a uniform impact. It negatively affects both velocity and penetration depth (β= -24.92 and -1.25, respectively). However, its influence on the hole diameter (Rx) is governed by complex interactions rather than a direct linear effect. As shown in Table 2, δ^2/d interacts significantly with both liner height (P=0.037) and top thickness (P=0.018). The mass distribution between the periphery and the core determines the projectile's radial expansion and stability.

Edelweiss Applied Science and Technology
ISSN: 2576-8484
Vol. 10, No. 4: 412-435, 2026
DOI: 10.55214/2576-8484.v10i4.12674

3.3.4. Effect of Charge Length

The charge length (l/d) exhibits a dualistic influence on warhead performance. Muzzle velocity (V) demonstrates a strong positive linear correlation ($\beta = +19.42$), reflecting the direct conversion of chemical energy into kinetic impulse. Conversely, penetration depth (S_x) follows a strictly quadratic relationship (P=0.007 for the squared term), indicating a clear saturation phenomenon. This suggests that extending the charge beyond a critical threshold yields diminishing returns, where additional explosive mass contributes to parasitic weight rather than enhancing shock wave coupling or effective penetrator formation.

4. Optimization Strategy

Based on the integrated analysis, the optimal design window is identified by maximizing the desirability function for high kinetic energy and deep penetration while maintaining a stable hole diameter. The recommended configuration lies within the range of minimal top thickness ($\delta_1/d \approx 0.033$), moderate liner height ($h/d \approx 0.22$–0.24), and a charge length ratio approaching the saturation point ($l/d \approx 1.25$).

4.1. Response Surface Analysis and Physical Interpretation

To comprehensively elucidate the physical mechanisms governing EFP formation, the explicit second-order regression models derived in Section 3.2 (Eqs. 8–10) were utilized to generate response surface plots. The visualization strategy was tailored to the dominant statistical features of each model: a 3D surface plot for muzzle velocity (V) to emphasize gradient sensitivity, a 3D interaction plot for hole diameter (R_x) to visualize synergistic effects, and a contour plot for penetration depth (S_x) to delineate the local optimization region.

Based on Equation (8), the sensitivity of muzzle velocity to geometric variations is illustrated in Fig, which presents the 3D response surface as a function of liner top thickness (δ_1/d) and liner height (h/d). The topology is characterized by a precipitous, monotonic decline along the δ_1/d axis, providing visual confirmation of the overwhelming negative coefficient identified in the ANOVA ($\beta = -297.0$). This steep gradient indicates that the linear apex functions as the primary inertial barrier to acceleration. Furthermore, a slight convexity is observable at the lower bounds of δ_1/d, reflecting the positive quadratic term; this suggests that the marginal utility of thinning the liner increases non-linearly as it approaches structural limits. Conversely, the influence of liner height manifests as a comparatively gentle slope, reinforcing the conclusion that kinematic performance is predominantly thickness-driven.

Edelweiss Applied Science and Technology
ISSN: 2576-8484
Vol. 10, No. 4: 412-435, 2026
DOI: 10.55214/2576-8484.v10i4.12674

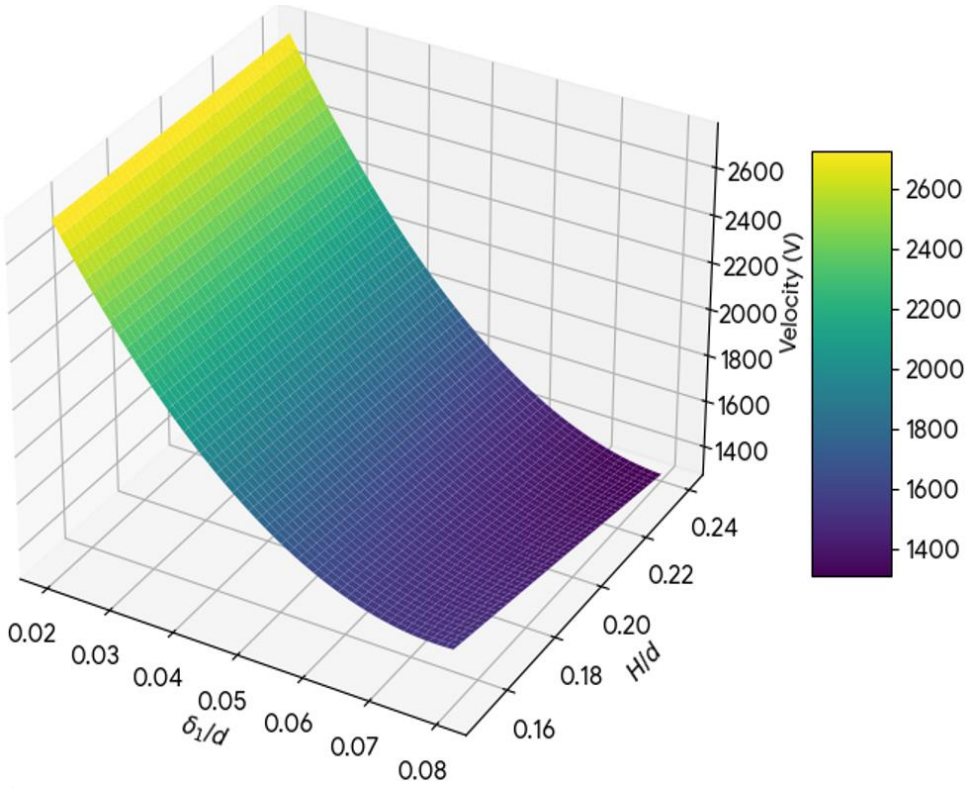

Figure 10.
3D response surface plot illustrating the interactive effect of liner height and top thickness on velocity.

In contrast to the linear dominance observed in velocity, the response surface for hole diameter (R_x), generated from Equation (9) and depicted in Fig, exhibits a distinct saddle-like geometry. This non-planar topography serves as the visual signature of the significant interaction between liner height and top thickness. The plot reveals a conditional dependency where the impact of top thickness relies heavily on the liner height. While variations in top thickness have a negligible impact at low liner heights ($h/d \approx 0.16$), increased top thickness significantly expands the hole diameter for taller liners ($h/d > 0.22$). Physically, this implies that slender projectiles require a robust apex to provide sufficient inertial confinement, thereby preventing radial collapse and ensuring a functional hole size for target interaction.

Edelweiss Applied Science and Technology
ISSN: 2576-8484
Vol. 10, No. 4: 412-435, 2026
DOI: 10.55214/2576-8484.v10i4.12674

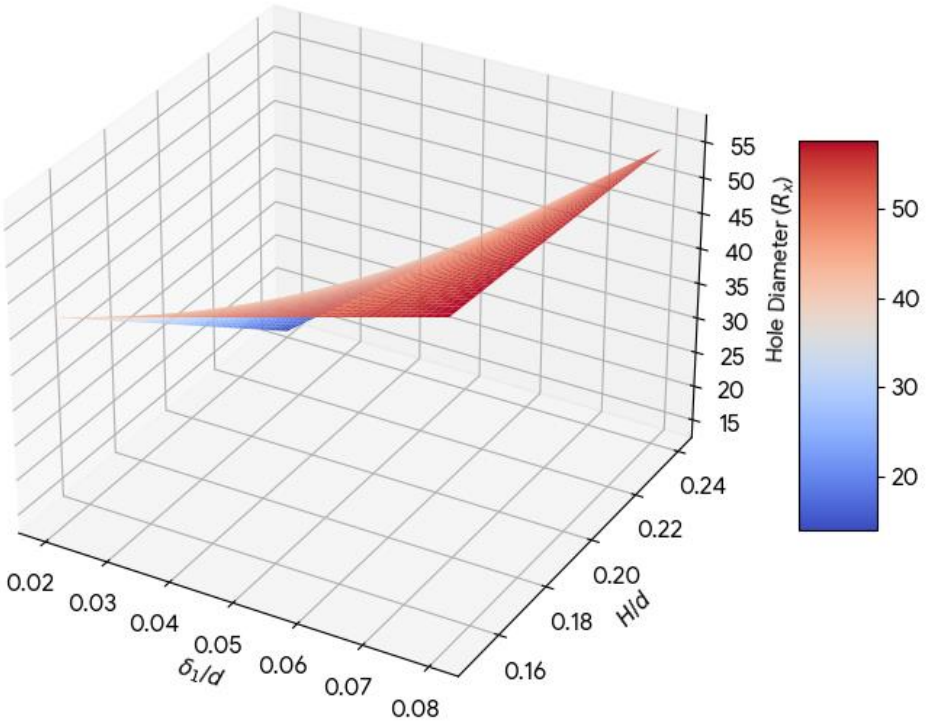

Figure 11.
3D response surface plot illustrating the interactive effect of liner height and top thickness on Hole Diameter.

Finally, the optimization landscape for penetration depth (S_x) is visualized in Figure via a contour plot derived from Equation (10), mapping liner height against charge length (l/d). Unlike the monotonic slopes associated with velocity, this plot displays a series of concentric rings narrowing toward a central stationary point, indicating a region of maximum performance. The contours along the horizontal axis demonstrate that penetration capabilities increase with charge length only up to a critical threshold ($l/d \approx 1.25$) before diminishing. This trend validates the negative quadratic term found in the regression model (Eq. 10) and suggests a saturation point where shock wave coupling efficiency reaches a hydrodynamic limit. Consequently, extending the charge beyond this point contributes primarily to blast overpressure rather than effective liner collapse. Similarly, the vertical axis demarcates an optimal height range of 0.22 to 0.24; deviating from this window results in either insufficient rod mass or excessive velocity loss, moving the design out of the optimal performance zone.

Edelweiss Applied Science and Technology
ISSN: 2576-8484
Vol. 10, No. 4: 412-435, 2026
DOI: 10.55214/2576-8484.v10i4.12674

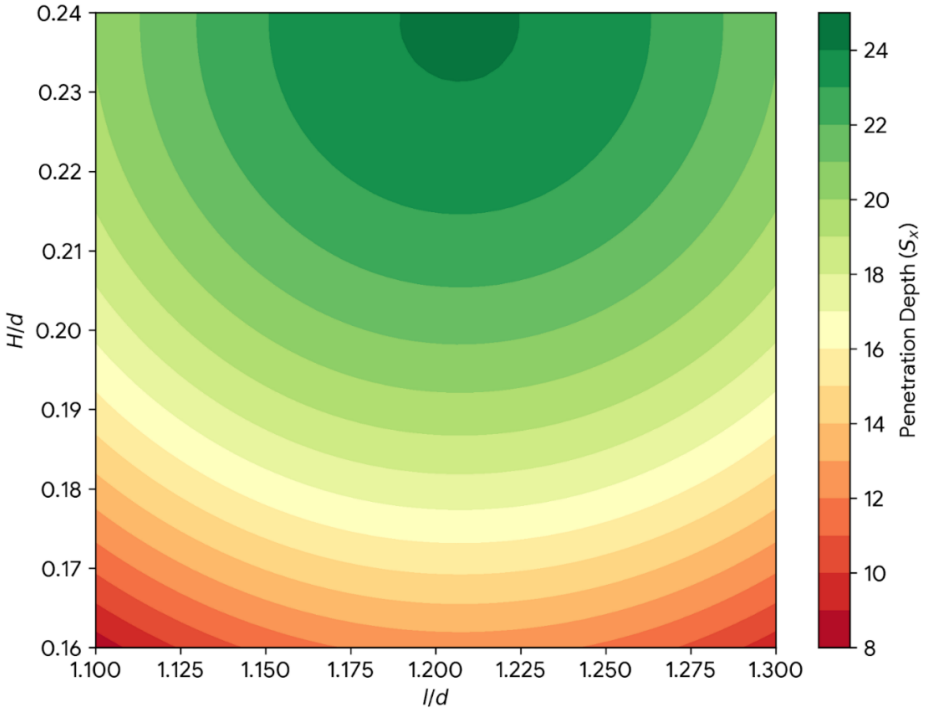

Figure 12.
Contour plot illustrating the interactive effect of liner height and charge length on Penetration Depth.

4.2. Constrained Multi-objective Optimization

4.2.1. Optimal Configuration based on Desirability Function

Initial unconstrained optimization attempts suggested minimizing the linear top thickness to its extreme lower limit ($\delta_1/d = 0.022$) to achieve a theoretical maximum velocity of approximately 2787 m/s. However, preliminary validation simulations indicated that such extreme thinness leads to structural instability (fracture) during the acceleration phase, causing large deviations between the regression model and physical reality. To ensure a robust design with high predictive reliability, a constrained optimization strategy was adopted. The lower bound of the top thickness was restricted to $\delta_1/d \geq 0.032$ to guarantee structural integrity. Under this constraint, the goal remained to simultaneously maximize Muzzle Velocity (V), Penetration Depth (S_x), and Hole Diameter (R_x) with equal importance.

Based on these refined boundary conditions, multi-objective optimization was executed using the desirability function approach. As illustrated in Figure , the global optimal solution was identified with a Composite Desirability of $D = 0.7332$, indicating a highly favorable balance among conflicting objectives.

Edelweiss Applied Science and Technology
ISSN: 2576-8484
Vol. 10, No. 4: 412-435, 2026
DOI: 10.55214/2576-8484.v10i4.12674

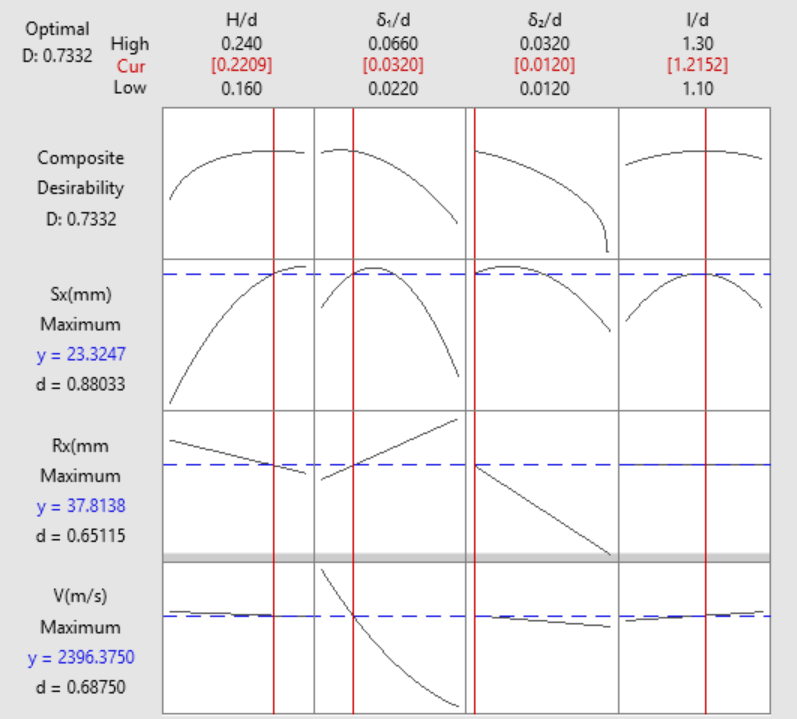

Figure 13.
Composite desirability profiles for the global optimal solution.

The predicted optimal parameters and their corresponding performance metrics, along with the 95% Prediction Intervals (PI), are summarized in Table 4.

Table 4.
Optimized design parameters with geometric constraints.

Parameter	Optimal Value	Response	Predicted (RSM)	95% PI
h/d	0.221	V	2396 m/s	(2358, 2435)
δ_1/d	0.032	S_x	23.32 mm	(19.69, 26.96)
δ_2/d	0.012	R_x	37.81 mm	(33.58, 42.05)
l/d	1.215			

This constrained approach results in a slightly reduced muzzle velocity compared to the unconstrained theoretical maximum (≈ 2396 m/s vs. ≈ 2787 m/s). However, this calculated reduction is strategic and yields significant physical benefits. Primarily, the slight increase in liner thickness (δ_1/d = 0.032) and height (h/d = 0.221) provides greater mass for the formation of the penetrator rod. Consequently, the predicted penetration depth (S_x) improved significantly from 21.85 mm (unconstrained) to 23.32 mm. Furthermore, by operating within this structurally safer regime, the discrepancy between the statistical model and physical behavior is minimized, ensuring that the predicted performance is mechanically achievable in practice. Ultimately, the design achieves a highly effective hydrodynamic balance: a high-velocity impact (≈ 2396 m/s) sufficient to overcome target resistance, combined with a maximized rod length for deep penetration and a large crater (R_x ≈ 37.8 mm) for severe behind-armor effects.

4.2.2. Numerical Verification of the Optimal Design

To rigorously validate the reliability of the constrained optimization strategy, a high-fidelity confirmatory simulation was executed in Ansys Autodyn using the precise global optimal parameters derived from the Response Surface Model (h/d=0.221, δ_1/d=0.032, δ_2/d=0.012, l/d=1.215). The initial

Edelweiss Applied Science and Technology
ISSN: 2576-8484
Vol. 10, No. 4: 412-435, 2026
DOI: 10.55214/2576-8484.v10i4.12674

objective was to assess the prediction accuracy of the statistical Minitab model against the complex multi-physics simulation. To ensure the extended penetration channel could be fully captured without rear-boundary interference, the numerical target was modeled as a 50 mm thick solid steel plate.

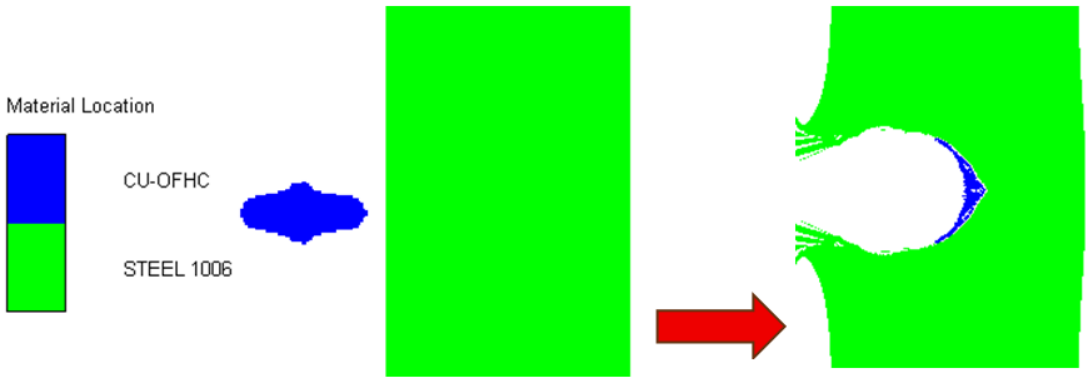

Figure 14.
Formation morphology and penetration channel in a 50 mm steel target for the optimized EFP configuration.

The transient formation process and the subsequent terminal ballistic interaction are visually captured in Figure 14. The explicit dynamics simulation demonstrates that the optimized EFP successfully collapses into a highly cohesive, elongated slug without exhibiting any signs of premature fragmentation. Upon impact with the 50 mm steel target, the penetrator generates a deep, well-defined cylindrical channel. This qualitative morphological evidence confirms that the constrained geometric parameters effectively balance inertial mass and kinetic energy. To further validate this physical behavior, the quantitative performance metrics extracted from the simulation must be compared against the statistical predictions.

Table 5.
Comparison between statistical prediction and explicit dynamics simulation for the optimal design.

Performance Metric	Minitab Prediction	Autodyn Simulation	Deviation
Muzzle Velocity (V)	2396.0 m/s	2405.0 m/s	+ 0.37 %
Hole Diameter (R_c)	37.8 mm	31.0 mm	- 18.0 %
Penetration Depth (S_c)	23.3 mm	29.0 mm	+ 24.4 %

As summarized in Table 5, the comparative data reveal profound insights into high-velocity penetration mechanics. In terms of kinematics, the Autodyn simulation yielded a muzzle velocity of 2405 m/s, demonstrating remarkable agreement with the Minitab-predicted value of 2396 m/s (a negligible error of 0.37%). This confirms the exceptional fidelity of the second-order regression model in calculating the explosive energy transfer. However, a significant and physically meaningful deviation was observed in the lethality metrics. The explicit dynamics simulation recorded a much deeper penetration of 29.0 mm (+24.4%) and a narrower hole diameter of 31.0 mm (-18.0%) compared to the statistical predictions. This discrepancy is not a computational artifact but a manifestation of high-strain-rate fluid-like behavior: at extreme hypervelocities (V > 2400 m/s), the penetrator slug experiences severe dynamic axial stretching and radial contraction (the necking effect). While the Minitab regression model trained on data from lower-velocity regimes extrapolated a wider crater, the physical simulation correctly captured this aerodynamic elongation. Consequently, the stretched morphology concentrates the kinetic energy over a smaller cross-sectional area, drastically reducing penetration resistance and driving the projectile significantly deeper into the 50 mm steel target than statistically anticipated.

Edelweiss Applied Science and Technology
ISSN: 2576-8484
Vol. 10, No. 4: 412-435, 2026
DOI: 10.55214/2576-8484.v10i4.12674

4.2.3. Performance Comparison with Baseline Designs

To evaluate the practical advantages of the optimized design, its simulated performance on a 20 mm steel target was compared against the experimental data of two baseline configurations: Case 2 (uniform-thickness liner) and Case 1 (variable-thickness liner). Because Case 1 achieved complete perforation of the 20 mm target, penetration depth (S_x) could not be used as a comparative metric. Consequently, the assessment focused on muzzle velocity (V) and hole diameter (R_x), which characterize the kinetic energy and damage morphology, respectively. The comparative results are summarized in Table 6 and graphically represented in Figure 15.

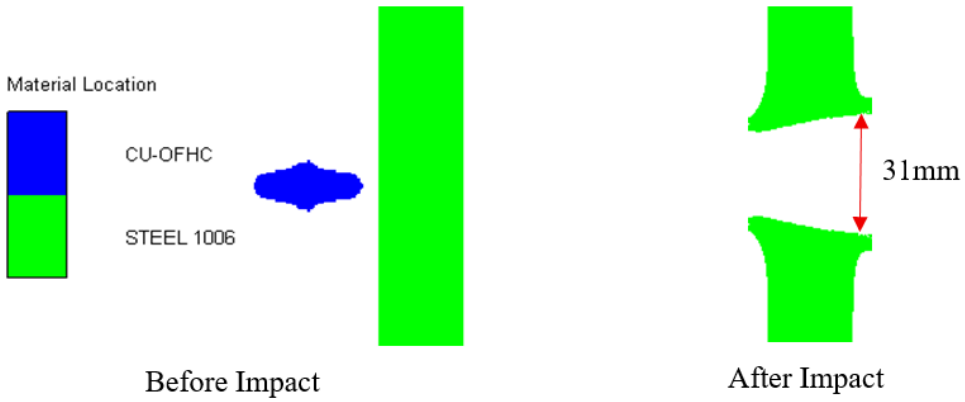

Figure 15.
Comparative analysis of muzzle velocity and hole diameter between baseline empirical designs and the optimized configuration.

The quantitative data indicate a significant kinematic improvement for the algorithmically derived configuration. The optimized design achieved a velocity of 2405 m/s, representing an increase of 14.7% compared to the variable-thickness design (Case 1) and 34.9% compared to the uniform-thickness design (Case 2). By strategically reducing the apex thickness ($\delta_1/d = 0.032$) while maintaining the overall liner height ($h/d = 0.221$), the optimization process minimized parasitic mass at the pole. This structural refinement facilitated a more efficient transfer of explosive shockwave energy into directed kinetic impulse, enhancing the projectile's acceleration.

Table 6.
Performance comparison between baseline designs and optimized configuration.

Metric	Case 1 (Exp)	Case 2 (Exp)	Optimized Design	Difference (vs. Case 1)	Difference (vs. Case 2)
Velocity (V)	2096.0 m/s	1783.0 m/s	2405.0 m/s	+ 14.7 %	+ 34.9 %
Hole Dia. (R_x)	37.7 mm	26.3 mm	31.0 mm	- 17.8 %	+ 17.9 %

Regarding penetration morphology, the hole diameter (R_x) of the optimized model was 31.0 mm. This dimension represents a highly effective morphological balance: it exhibits a 17.9% increase compared to the uniform-thickness baseline (Case 2, 26.3 mm), while showing a 17.8% reduction relative to the variable-thickness baseline (Case 1, 37.7 mm). Rather than indicating performance degradation, the reduction compared to Case 1 is a direct physical consequence of dynamic necking. At high velocities exceeding 2400 m/s, the velocity gradient along the projectile axis induces severe axial stretching. This deformation mechanism naturally reduces the penetrator's radial cross-section while increasing its overall length. According to hydrodynamic penetration principles, such an elongated profile with a higher length-to-diameter ratio minimizes the target's resistance cross-section. This optimal morphology effectively avoids the excessive radial mass dispersion seen in Case 1, while concurrently

Edelweiss Applied Science and Technology
ISSN: 2576-8484
Vol. 10, No. 4: 412-435, 2026
DOI: 10.55214/2576-8484.v10i4.12674

overcoming the limited crater generation of the slower Case 2. Ultimately, this configuration optimally concentrates the projectile's mass and momentum along the primary penetration axis, directly contributing to the enhanced penetration capability verified on the 50 mm steel plate in Section 4.2.2.

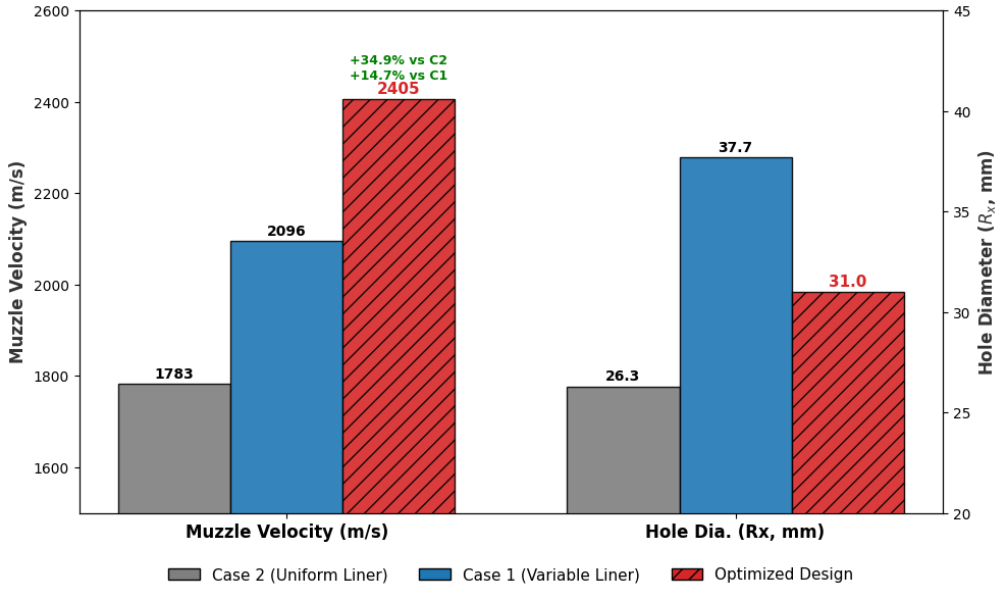

Figure 16.
Quantitative Comparison: Baselines vs. Optimized Design.

5. Conclusion

This study has successfully established a high-precision, multi-objective optimization framework for EFP by integrating CCD with advanced explicit dynamics simulations. By systematically exploring the quadratic interactions between four dimensionless geometric parameters (h/d, δ_1/d, δ_2/d, l/d), the research provides a rigorous understanding of the nonlinear trade-offs governing warhead lethality.

The key findings and contributions are summarized as follows:

1. Quantification of Parametric Sensitivity: ANOVA confirmed that the linear top thickness (δ_1/d) primarily dictates kinematic performance (>98% contribution to velocity variance), while linear height (h/d) controls morphological stability. Additionally, the response surface analysis identified an energy saturation plateau at a charge length ratio of $l/d \approx 1.2$, beyond which efficiency diminishes.
2. Optimized Design Identification: The constrained optimization framework identified a superior geometric configuration (h/d=0.221, δ_1/d=0.032, δ_2/d=0.012, and l/d=1.215). Confirmatory simulations verified that this optimal design achieves a high velocity of 2405 m/s and a maximum penetration depth of 29.0 mm. This hydrodynamic elongation reduces penetration resistance, enabling the slug to penetrate 24.4% deeper than statistical predictions and outperforming empirical baselines by up to 34.9% in velocity.
3. Validation and Reliability: The numerical framework demonstrated exceptional predictive fidelity. Initial validation against static firing experiments yielded relative errors consistently below 6%. Furthermore, the confirmatory simulation of the optimal design showed a negligible 0.37% velocity deviation compared to the regression metamodels, proving the robustness of the methodology in capturing explosive energy transfer.
4. Practical Engineering Implications: The findings advocate for a "variable-thickness, constrained-height" design strategy to maximize EFP lethality while preventing premature fragmentation.

Edelweiss Applied Science and Technology
ISSN: 2576-8484
Vol. 10, No. 4: 412-435, 2026
DOI: 10.55214/2576-8484.v10i4.12674

The developed second-order regression models provide a reliable, computationally efficient tool for advanced warhead engineering, effectively overcoming the energy dispersion limitations of conventional trial-and-error testing.

The proposed optimization framework directly applies hydrodynamic principles to practical EFP warhead design. Future work will extend this methodology to evaluate alternative liner materials, such as tantalum and reactive alloys, and assess the dynamic effects of stand-off distance on composite armor penetration.

Transparency:

The authors confirm that the manuscript is an honest, accurate, and transparent account of the study; that no vital features of the study have been omitted; and that any discrepancies from the study as planned have been explained. This study followed all ethical practices during writing.

Copyright:

References

[1] W. P. Walters and J. A. Zukas, *Fundamentals of shaped charges*. New York: John Wiley & Sons, 1989.
[2] L. P. Orlenko, *Physics of explosion and impact*, 2nd ed. Moscow: Fizmatlit, 2008.
[3] J. Peng, J. Jiang, J. Men, H. Kang, X. Gao, and G. Yin, "Explosively formed projectile from stepped casing shaped charge: Formation mechanism of canted fins," *Journal of Energetic Materials*, vol. 42, no. 2, pp. 291-312, 2024. https://doi.org/10.1080/07370652.2022.2064937
[4] M. Mayseless, "Effectiveness of explosively formed projectiles against reactive armor," *Journal of Applied Mechanics*, vol. 78, no. 5, p. 051012, 2011.
[5] F. Zhang, C. Zhao, W. Feng, C. Ji, S. Lin, and X. Wang, "Numerical simulation study on collinear EFP from warhead with double layer liners penetrating into target," *Vibroengineering Procedia*, vol. 39, pp. 138-143, 2021. https://doi.org/10.21595/vp.2021.22214
[6] X. Zhu, "Microstructure evolution and deformation mechanism of tantalum–tungsten alloy liner under ultra-high strain rate by explosive detonation," *Materials*, vol. 15, no. 15, p. 5447, 2022.
[7] D. Bender and J. Carleone, *Tactical missile warheads*. Washington, DC: American Institute of Aeronautics and Astronautics (AIAA), 1993.
[8] J. A. Zukas, *Introduction to hydrocodes*. Amsterdam, Netherlands: Elsevier, 2004.
[9] D. J. Benson, "Computational methods in Lagrangian and Eulerian hydrocodes," *Computer Methods in Applied Mechanics and Engineering*, vol. 99, no. 2-3, pp. 235-394, 1992. https://doi.org/10.1016/0045-7825(92)90042-I
[10] M. Liu, Z. Zhang, and Y. Li, "Smoothed particle hydrodynamics (SPH) for modeling fluid-structure interactions," *Applied Ocean Research*, vol. 59, pp. 178–189, 2013.
[11] D. Si, Z. Pan, and H. Zhang, "Determination method of mesh size for numerical simulation of blast load in near-ground detonation," *Defence Technology*, vol. 38, pp. 111-125, 2024. https://doi.org/10.1016/j.dt.2023.08.004
[12] P. A. Salas, D. J. Benson, and S. Venkataraman, "Modeling error estimation in response prediction of multilevel composite systems using Bayesian networks," presented at the 52nd AIAA/ASME/ASCE/AHS/ASC Structures, Structural Dynamics and Materials Conference, 1906, 2011.
[13] G. R. Johnson and W. H. Cook, "Fracture characteristics of three metals subjected to various strains, strain rates, temperatures and pressures," *Engineering Fracture Mechanics*, vol. 21, no. 1, pp. 31-48, 1985. https://doi.org/10.1016/0013-7944(85)90052-9
[14] R. Castedo *et al.*, "Estimation of Jones-Wilkins-Lee parameters of emulsion explosives using cylinder tests and their numerical validation," *International Journal of Rock Mechanics and Mining Sciences*, vol. 112, pp. 290-301, 2018. https://doi.org/10.1016/j.ijrmms.2018.10.027
[15] ANSYS Autodyn User's Manual, "ANSYS Inc," 2021. https://www.ansys.com/products/structures/ansys-autodyn
[16] Z. Zhang, L. Qiao, and W. Li, "Numerical investigation on the formation and penetration behavior of explosively formed projectile (EFP) with variable thickness liner," *Symmetry*, vol. 13, no. 8, p. 1342, 2021.
[17] Y. Wang, "Cost-effective design of EFP warheads using numerical simulation," *Journal of Energetic Materials*, vol. 33, no. 2, pp. 112–125, 2015.
[18] C.-b. Hu and X.-b. Zhang, "Influence of multiple structural parameters on interior ballistics based on orthogonal test methods," *Defence Technology*, vol. 15, no. 5, pp. 690-697, 2019. https://doi.org/10.1016/j.dt.2019.06.014

[19] M. Park, J. Yoo, and D.-T. Chung, "An optimization of a multi-layered plate under ballistic impact," *International Journal of Solids and Structures*, vol. 42, no. 1, pp. 123-137, 2005. https://doi.org/10.1016/j.ijsolstr.2004.07.008

[20] X. Li, M. Xu, J. Wang, and H. Xu, "Study on grain refinement of copper-based liner by vacuum gradient heat treatment process using response surface methodology," *Journal of Materials Research and Technology*, vol. 15, pp. 2345-2354, 2021. https://doi.org/10.1016/j.jmrt.2021.09.066

[21] D. C. Montgomery, *Design and analysis of experiments*, 9th ed. Hoboken, NJ: John Wiley & Sons, 2017.

[22] N. Senthilnathan and S. Vasantha, "Trends and usage pattern of SPSS and Minitab software in scientific research," *International Journal of Research in Library Science*, vol. 8, no. 1, pp. 108–117, 2022.

[23] T. T. Allen, *Software overview and methods review: Minitab. Introduction to engineering statistics and lean six sigma*. Cham, Switzerland: Springer, 2019.

[24] Y.-T. Jou, W.-T. Lin, W.-C. Lee, and T.-M. Yeh, "Integrating the Taguchi method and response surface methodology for process parameter optimization of the injection molding," *Applied Mathematics & Information Sciences*, vol. 8, no. 3, pp. 1277–1285, 2014.

[25] W.-H. Chen *et al.*, "A comprehensive review of thermoelectric generation optimization by statistical approach: Taguchi method, analysis of variance (ANOVA), and response surface methodology (RSM)," *Renewable and Sustainable Energy Reviews*, vol. 169, p. 112917, 2022. https://doi.org/10.1016/j.rser.2022.112917

[26] A. Kumar and V. Gulati, "Experimental investigation and optimization of surface roughness in negative incremental forming," *Measurement*, vol. 131, pp. 419-430, 2019. https://doi.org/10.1016/j.measurement.2018.08.078

[27] G. E. P. Box and K. B. Wilson, "On the experimental attainment of optimum conditions," *Journal of the Royal Statistical Society: Series B Methodological*, vol. 13, no. 1, pp. 1–45, 1951.

[28] R. Echempati, B. Kwintiana, M. E. Krueger, and D. Roller, "Optimal central composite design for manufacturing simulation of 0.50 caliber projectile," *ASME 2011 International Mechanical Engineering Congress and Exposition*, vol. 3, pp. 141-150, 2011.

[29] S. Kim *et al.*, "Topology optimization of reactive material structures for penetrative projectiles," *Defence Technology*, vol. 18, no. 7, pp. 1205-1218, 2022. https://doi.org/10.1016/j.dt.2021.05.001

[30] R. H. Myers, D. C. Montgomery, and C. M. Anderson-Cook, *Response surface methodology: Process and product optimization using designed experiments*. Hoboken, NJ: John Wiley & Sons, 2016.

[31] A. I. Khuri and S. Mukhopadhyay, "Response surface methodology," *Wiley Interdisciplinary Reviews: Computational Statistics*, vol. 2, no. 2, pp. 128-149, 2010. https://doi.org/10.1002/wics.73

[32] R. L. Mason, R. F. Gunst, and J. L. Hess, *Statistical design and analysis of experiments: With applications to engineering and science*. Hoboken, NJ: John Wiley & Sons, 2003.

[33] P. Dugard, J. Todman, and H. Staines, *Approaching multivariate analysis: A practical introduction*. London, UK: Routledge, 2023.

[34] J. Witzany, "A bayesian approach to backtest overfitting," *Available at SSRN 3002503*, p. 3002503, 2017.

[35] P. H. Quan and T. D. Thanh, "Numerical and experimental investigation of liner top thickness on the formation and penetration performance of explosively formed projectiles," *Vietnam Journal of Mechanics*, vol. 47, no. 4, pp. 364-380, 2025. https://doi.org/10.15625/0866-7136/23163

[36] P. H. Quan, V. M. Do, and D. D. Nguyen, "Experimental and numerical study on the influence of liner height on explosively formed projectiles," *Advances in Military Technology*, vol. 20, no. 1, pp. 55-68, 2025. https://doi.org/10.3849/aimt.01961

[37] S. P. Marsh, *LASL shock Hugoniot data*. Berkeley, CA: University of California Press, 1980.

[38] H. R. Couque, R. Boulanger, and F. Bornet, "A modified johnson-cook model for strain rates ranging from 103 to 105 s-1," *Journal de Physique IV (Proceedings)*, vol. 134, pp. 87–93, 2006. https://doi.org/10.1051/jp4:2006134015

[39] G. Hussain, A. Hameed, J. Hetherington, P. C. Barton, and A. Malik, "Hydrocode simulation with modified Johnson-Cook model and experimental analysis of explosively formed projectiles," *Journal of Energetic Materials*, vol. 31, no. 2, pp. 143–155, 2013. https://doi.org/10.1080/07370652.2011.606453

[40] P. J. Roache, *Verification and validation in computational science and engineering*. Albuquerque, NM: Hermosa Publishers, 1998.

[41] H. Q. Pham, V. M. Do, and D. T. Tran, "Experimental and numerical study on the influence of explosive charge length on the performance of explosively formed projectiles," *Vietnam Journal of Science, Technology and Engineering*, vol. 67, no. 1, pp. 54–59, 2025.

[42] M. R. Vaziri, M. Salimi, and M. A. Mashayekhi, "New calibration method for ductile fracture models as chip separation criteria in machining," *Simulation Modelling Practice and Theory*, vol. 18, no. 9, pp. 1286–1296, 2010. https://doi.org/10.1016/j.simpat.2010.05.003